

# A Novel and Open-Source Application for Vasculature Dataset Analysis and Visualization

Jacob Bumgarner (✉ [jrbumgarner@mix.wvu.edu](mailto:jrbumgarner@mix.wvu.edu))

West Virginia University <https://orcid.org/0000-0002-0387-9263>

Randy Nelson

West Virginia University

---

## Article

**Keywords:** Vasculature analysis, 3D vasculature, 2D vasculature, vasculature visualization, vascular networks

**Posted Date:** June 11th, 2021

**DOI:** <https://doi.org/10.21203/rs.3.rs-608609/v1>

**License:** © ⓘ This work is licensed under a Creative Commons Attribution 4.0 International License.

[Read Full License](#)

---

1 Submitted to Nature Methods on 10 June 2021

2  
3  
4  
5  
6  
7  
8  
9  
10  
11  
12  
13  
14  
15  
16 A Novel and Open-Source Application for Vasculature Dataset Analysis and Visualization

17  
18 Jacob R. Bumgarner\* and Randy J. Nelson

19  
20 Department of Neuroscience  
21 Rockefeller Neuroscience Institute  
22 West Virginia University  
23 Morgantown, WV 26505 USA  
24  
25  
26  
27  
28  
29  
30

31 \*To whom correspondence should be addressed:

32 [jrbumgarner@mix.wvu.edu](mailto:jrbumgarner@mix.wvu.edu)

34 **Abstract**

35           Vascular networks can dictate and indicate states of health and disease. Structural analyses of  
36 these networks can facilitate improved understanding of disease states. Recent advances in preclinical  
37 imaging techniques and segmentation software have led to the generation of large-scale vasculature  
38 datasets. However, these advances have not been accompanied by the development of modernized,  
39 open-source analysis software packages. Here we describe VesselVio, an application developed to  
40 analyze and visualize pre-segmented 2D and 3D vasculature datasets. Vasculature datasets can be  
41 loaded and analyzed with custom parameters to extract numerous quantitative whole-network and  
42 individual segment features. Visualization of results and accuracy inspections can be conducted using  
43 the interactive visualization tool. The utility and compatibility of VesselVio is demonstrated via the  
44 analysis of 3D inferior colliculus segmentations from female and male mice as well as the analysis of  
45 2D retinal fundus images of control, glaucomatous, and diabetic retinopathy patients.

46

47 **Keywords**

48 Vasculature analysis, 3D vasculature, 2D vasculature, vasculature visualization, vascular networks.

49

## 50 Introduction

51 Microvascular networks serve vital roles in the maintenance of cellular function in all tissue by  
52 providing finely tuned routes for the delivery and clearance of nutrients and waste, signaling molecules,  
53 and trafficking immune cells. Often, vascular networks become disorganized or impaired by diseases  
54 or illnesses, such as COVID-19<sup>1</sup>, diabetes<sup>2</sup>, stroke<sup>3</sup>, or Alzheimer's disease<sup>4</sup>, which can lead to  
55 compounding detrimental health consequences. Accordingly, detailed characterization of the distinct  
56 structural features of these networks may enable improved comprehension and identification of  
57 underlying pathological conditions.

58 In recent years, high-resolution and large-scale 3D vasculature dataset generation has been  
59 facilitated by continued developments of light sheet fluorescent microscopy (LSM)<sup>5-7</sup> and micro  
60 computed tomography imaging techniques ( $\mu$ CT)<sup>8,9</sup>. Simultaneously, constant improvements in  
61 computational power and availability of powerful programming languages provide greater means by  
62 which to process and extract detailed features from the resulting datasets. Together, micron-scaled  
63 resolution imaging and powerful computational tools can be utilized to reveal intricate details of  
64 microvascular networks that will lead to an improved understanding of microvascular structure, function,  
65 and remodeling in health and disease.

66 However, ongoing advancements in imaging technologies and open-source image  
67 segmentation software for 3D vasculature datasets<sup>6,7,10</sup> have not yet been accompanied by publication  
68 of free and easily accessible analysis software toolkits. For example, there are several freely available  
69 older analysis tools, but they are unable to extract features from 3D datasets<sup>11,12</sup>. Other modern open-  
70 access analysis packages have similar 2D limitations<sup>13-15</sup>. Existing open-source analysis tools and  
71 software packages capable of analyzing 3D vasculature have several limitations. Several of these tools  
72 can extract 3D network characteristics, yet they depend on simple centerline analyses, provide limited  
73 feature output, and markedly over-label branchpoints, producing inaccurate results<sup>7,16</sup>. Other modern  
74 analysis packages that extract more accurate<sup>6,17</sup> and detailed features<sup>18,19</sup> from 3D vascular networks

75 require experience with programming or interaction with terminals, potentially leading to unwelcome  
76 usage barriers and steep learning curves for researchers. Many publications also make use of private  
77 code or proprietary software for feature extractions<sup>20-22</sup>. In these instances, limited code availability and  
78 high software prices can hinder widespread analysis access. Thus, there is an apparent void for a freely  
79 accessible tool for 3D vasculature dataset analysis.

80 Here we present *VesselVio*, an open-source application for the analysis and visualization of 2D  
81 and 3D vasculature datasets. We created this application by first developing backend pipelines for  
82 dataset analysis and visualization with several novel feature extraction techniques. Both backend  
83 pipelines leverage high-level python libraries, just-in-time compilers, and parallel processing for rapid,  
84 detailed feature extraction and complementary visualization of datasets. We then designed a stand-  
85 alone and downloadable front-end application to wrap these pipelines with ease of use in mind. To test  
86 the performance and utility of *VesselVio*, we analyzed ground-truth synthetic vascular datasets, and we  
87 analyzed 2D retinography datasets and 3D vasculature datasets generated by  $\mu$ CT, LSM, and MRI  
88 imaging.

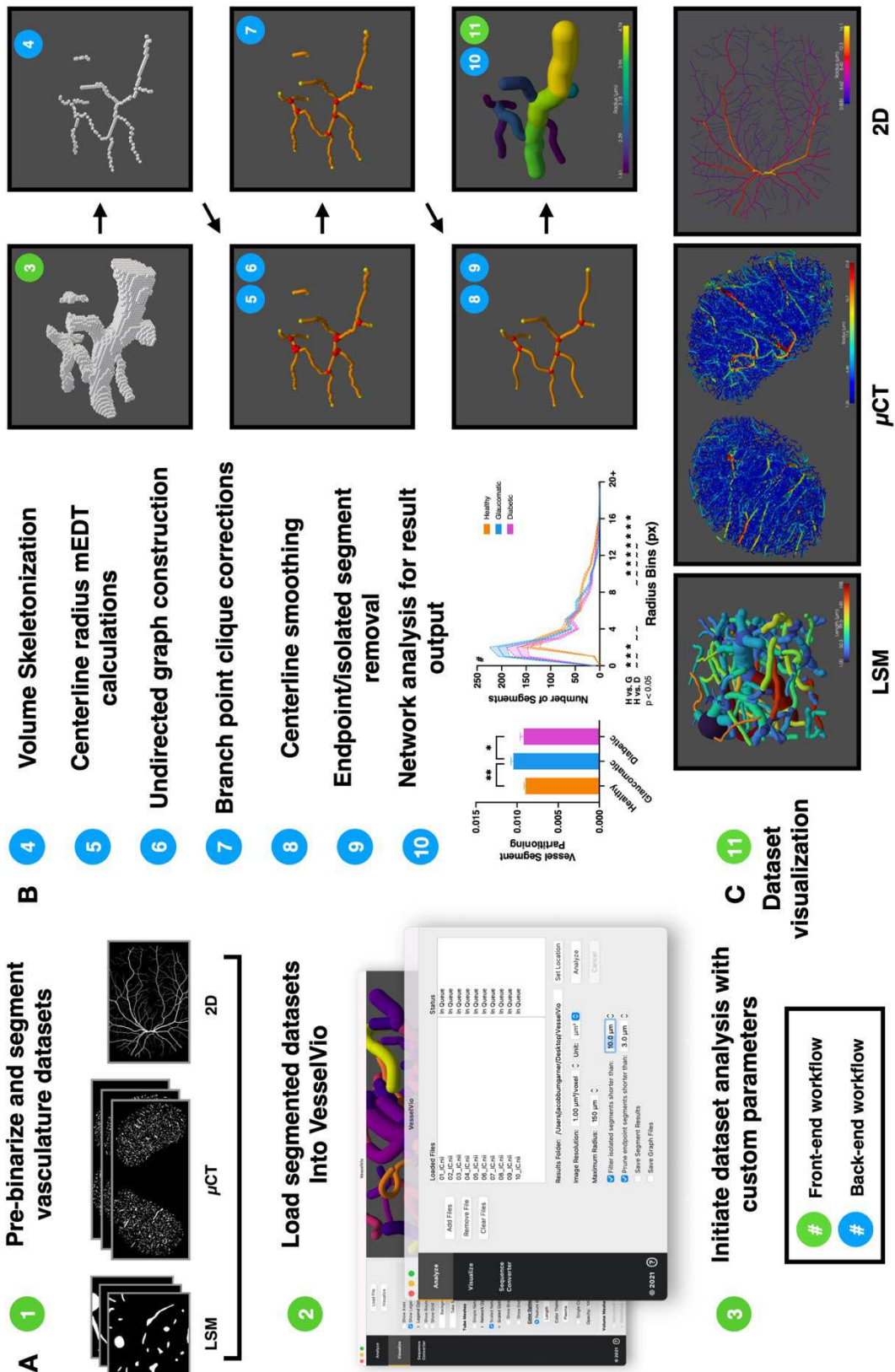
## 90 Results

### 91 *Centerline Extraction and Graph Theory Enable Detailed Vascular Network Feature Extraction*

92 We sought to build an open-source application that allows users to extract numerous quantitative  
93 features from 2D and 3D vascular networks. Different imaging techniques can produce varying qualities  
94 of raw images that require unique vessel detection and thresholding processes. Because of this,  
95 VesselVio was developed for vascular datasets that have already been binarized and segmented,  
96 enabling it to be used with datasets of any imaging origin (Figure 1A). This development choice enabled  
97 analysis pipeline optimization for increased accuracy and speed of feature identification. The  
98 visualization component for the program enables researchers to examine their results alongside original  
99 volume meshes for accuracy inspection.

100 The features of a vascular network can be extracted by identifying centerlines of the network  
101 and creating undirected graphs of the centerline points<sup>23,24</sup>. To locate vessel centerlines, a widely used  
102 2D and 3D thinning algorithm for binarized images was employed to extract the skeleton of our  
103 datasets<sup>25</sup>. Edge-connectivity of the skeleton points is identified and used to create an undirected graph  
104 with the resulting edges and points,  $G = (V, E)$ . Following initial graph construction, the datasets follow  
105 a series of correction processes to filter out spurious branchpoint labels, smooth centerlines, and  
106 remove isolated/endpoint segments at user-defined size (Figure 1B). These initial processing stages  
107 enable downstream quantifications of network and segment features (Figure 1C).

108 **Figure 1** – Overview of the analysis and visualization pipelines of VesselVio. **a**, Pre-segmented  
109 datasets are loaded into the program where analyses can be conducted using custom analysis and  
110 feature export parameters. **b**, Centerlines are extracted from the loaded datasets, and undirected  
111 graphs are created with the resulting vertices and edges. Centerlines are smoothed, spurious branch  
112 points are filtered, and segments are filtered prior to result extraction. **c**, The resulting datasets can  
113 be visualized for inspection of the accuracy and quality of results.  
114



## Endpoints and Branchpoint Clique Filtering

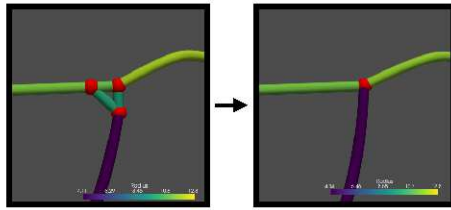
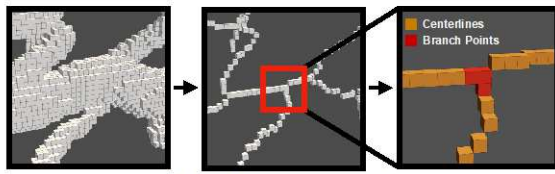
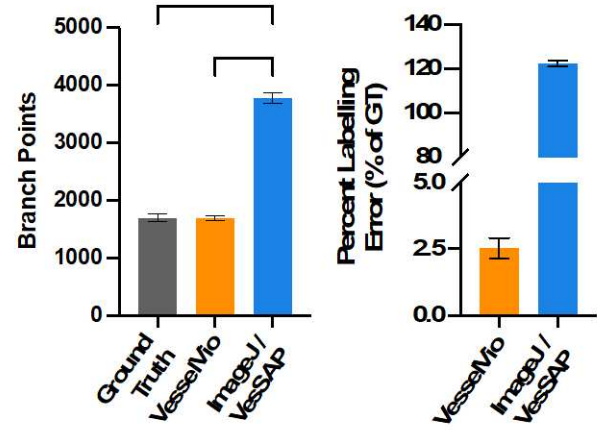
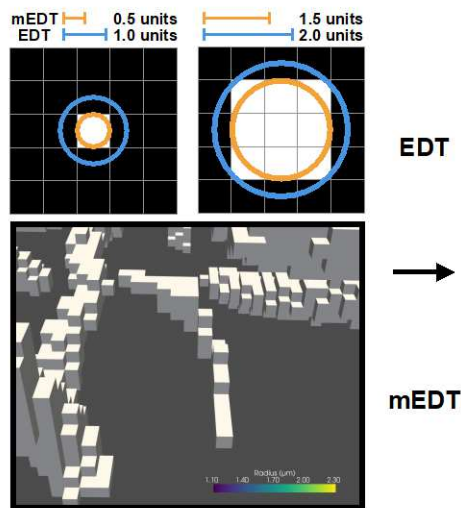
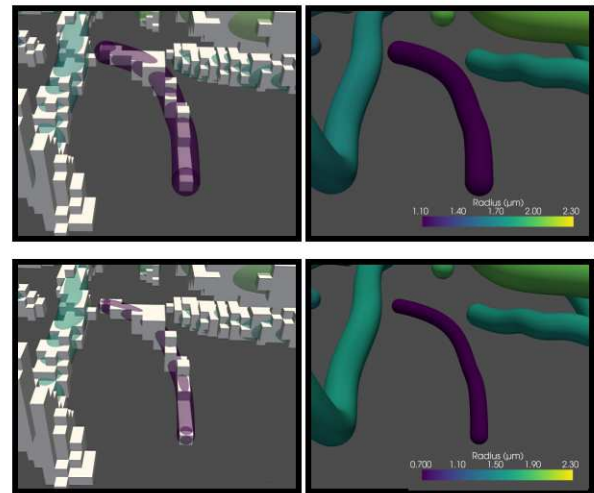
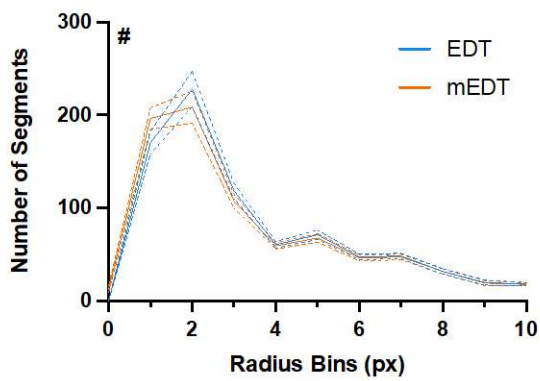
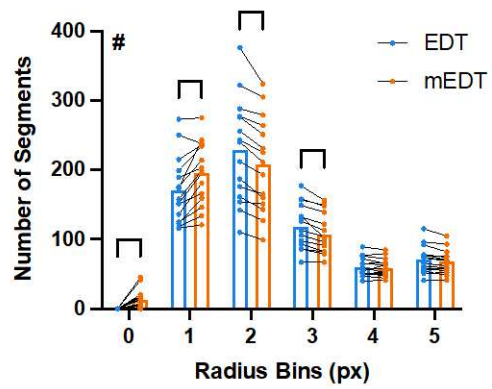
After graph construction, network endpoints and branchpoints are identified by examining the degree of connectivity of the centerline vertices (Figure 2A). Centerline neighbor 26-connectivity is a commonly used method for branchpoint and endpoint identification<sup>7,16,18</sup>. Although endpoints can be accurately detected using this technique, branchpoints are spuriously labeled and counts become artificially inflated (Figure 2B). Some programs allow for interactive user input to correct incorrectly labelled segments, centerlines, or branchpoints (e.g., Imaris<sup>8</sup>). However, manually correcting branchpoints in 3D datasets can become tedious and time-intensive, particularly when datasets are several gigabytes large. Because VesselVio is designed for automated analysis without user guidance, a set of algorithms were implemented to automatically filter incorrectly identified branchpoints from analyzed datasets.

Spuriously labelled branchpoints form small loops in the constructed graphs, otherwise known as *cliques*. Branchpoint cliques can be identified by filtering the graph of endpoints, 2-degree vertices, and single or two-component branchpoints. These cliques contain candidate branchpoints with one or more loops generated by between-edges (Figure 2A). Previous techniques used to eliminate spurious branchpoint labels rely on parent vessel orientations<sup>26</sup> or generate candidate weights based on 26-neighborhood connectivity<sup>27</sup>. Instead, VesselVio implements a series of filtering algorithms that apply branchpoint candidate weighting based on vertex radius, neighbor radius, and degree of connectivity (Supplementary Notes). Weighting candidates based on radius in addition to connectivity also mimics parent vessel hierarchy and improves calculations of segment radii.

To test our filters, a set of synthetically generated vasculature datasets with branchpoint labels were analyzed and results were compared to previous programs<sup>16,28</sup>. Labeled branchpoints from these

139 datasets were considered as ground truths. VesselVio clique filtering resulted in a mean 97.5%  
140 accuracy of branchpoint labeling by removing an average of 99.6 % of identified cliques in the datasets  
141 ( $N = 20$ ) (Supplementary Notes; Supplementary Data 1). The hierarchical branchpoint filtering of  
142 VesselVio with a mean of 2.5 % error outperforms the mean 122.2 % error of previous techniques  
143 (Figure 2B). Further, application of the filtering algorithms resulted in correction of 99.7% ( $N = 10$ ) and  
144 99.9% ( $N = 45$ ) of the identified branchpoint cliques in the 3D and 2D datasets that are analyzed below,  
145 respectively (Supplementary Data 1).

146 **Figure 2** – Spurious branch point filtering and modified radius calculations. **a**, Spuriously labeled branch  
147 points from 26-edge connectivity are filtered by weighting the radius of the candidate points and their  
148 neighbors. **b**, Branch point filtering compared to ground-truth labeled synthetic vasculature datasets ( $n$   
149 = 20). **c**, Modified Euclidean distance transform (mEDT) radius calculations for vessels with 1D nearest  
150 neighbors. **d**, Comparisons between EDT and mEDT radius calculations for an edge-vessel with single-  
151 voxel width at numerous points. **e**, Comparison of the distribution of segments along 0-10 px radius  
152 bins from the glaucomatous HRF images ( $n = 15$ ). **f**, Repeated-measures analysis of the change in  
153 radius differences in the 0-5 px radius bins from EDT to mEDT. Data are represented as mean  $\pm$   
154 SEM. **b**, Data analyzed using a one-way ANOVA. **e-f**, Data analyzed using a repeated measures two-  
155 way ANOVA. Multiple comparisons conducted using Tukey's test. # - Main effect of measurement  
156 method. \*\*\* -  $p < 0.001$ , \*\*\*\* -  $p < 0.0001$ .

**A****B****C****D****E****F**

## 158 **Identifying Segment Radii Based on Voxel Edges**

159 Several techniques exist for identifying vessel radii. One technique involves recording the largest  
160 maximally inscribed spheres that can rest within mesh vessel centerline points<sup>29,30</sup>, but this technique  
161 often depends on the creation of directed graphs (i.e., manually directed vessel hierarchy) and thus  
162 was not suitable for an automated pipeline. A similar method identifies the Euclidian distance between  
163 a vessel centerline and the center of the nearest non-vessel neighbor<sup>6,31</sup>. However, one pitfall to this  
164 approach is that vessels with near-resolution or at-resolution radii are incorrectly sized when their  
165 closest non-vessel neighbor is located along the 1<sup>st</sup> dimension of individual axes (Figure 2C), leading  
166 to oversized single-pixel/-voxel vessels (Figure 2D). This issue is not as apparent for 2<sup>nd</sup> and 3<sup>rd</sup>  
167 dimension neighbors (Supplementary Figure 1). As such, a simple half-unit correction for 1D neighbors  
168 (6-connectivity) is implemented to preserve small-segment radii measurements (Figure 2C). This  
169 technique enables the identification of smaller segments within vascular datasets by removing artificial  
170 inflation of segment size along the first dimension (Figure 2E, F; Supplementary Data 2).

## 172 **VesselVio Feature Reporting**

173 Following the identification of branchpoints, endpoints, and centerline radii, individual vessel  
174 segments and their features can be isolated from vascular networks. These features include average  
175 length, radius, tortuosity, surface area, and volume. Segment information can be scaled to describe  
176 network features, including network volume and skeleton length, vessel segment partitioning, segment  
177 counts, and averages of segment features. Implementation of graph theory and graph file exports from  
178 VesselVio enables users to independently identify relevant network characterization metrics, such as  
179 cohesion, network diameter, or clustering coefficient measurements<sup>18</sup>. Lastly, by leveraging the same

180 back-end analysis pipeline with an additional mesh-construction stage, VesselVio can render vascular  
181 datasets for visualization and inspection of result accuracy (Figure 1C).

## 183 **VesselVio Quantification and Visualization**

### 184 **$\mu$ CT, LSM, and MRI Datasets**

185 To demonstrate VesselVio 3D compatibility, several datasets were analyzed. First,  
186 cerebrovascular resin casts of female and male CFW mice ( $n = 5$ ) were created as described  
187 previously<sup>8</sup>. Following tissue removal and subsequent osmication, the resulting vasculature casts were  
188 imaged using a  $\mu$ CT scanner at an isotropic resolution of  $2.7 \mu\text{m}^3$ . Next, the inferior colliculi (IC) were  
189 segmented and binarized as example datasets (Supplementary Video 1). As expected, the IC were  
190 densely vascularized with large peaks in small diameter vessels (Figure 3H); VesselVio analysis  
191 revealed numerous other vascular network features (Figure 3; Supplementary Video 2). In all, there  
192 were few sex differences in IC vasculature. However, female IC vasculature had longer segment  
193 lengths on average than males (Figure 3G; Supplementary Data 3).

194 Several other 3D vasculature datasets of varying imaging origins were also examined. First, a  
195 lymph node microvascular network imaged with confocal laser scanning microscopy was visualized to  
196 reveal complex capillary networks (Supplementary Video 3)<sup>22</sup>. Visualization and analysis tests were  
197 also demonstrated on sample datasets generated by LSM (Supplementary Video 3)<sup>7,10</sup>. Lastly, to  
198 demonstrate visualization capability with large-vessel networks, open-source composite datasets of  
199 susceptibility weighted imaging (SWI) and time-of-flight magnetic resonance angiography (ToF) from  
200 41 human subjects were utilized<sup>32</sup>. To visualize arterial and venous vasculature simultaneously, the  
201 SWI and ToF composites were thresholded, combined, and analyzed, revealing a complex cortical  
202 vascular topology (Supplementary Video 4). Together, the analysis of rodent cerebrovasculature,

rodent lymph node, and human cerebrovasculature datasets demonstrates VesselVio's compatibility with 3D datasets generated by various imaging techniques.

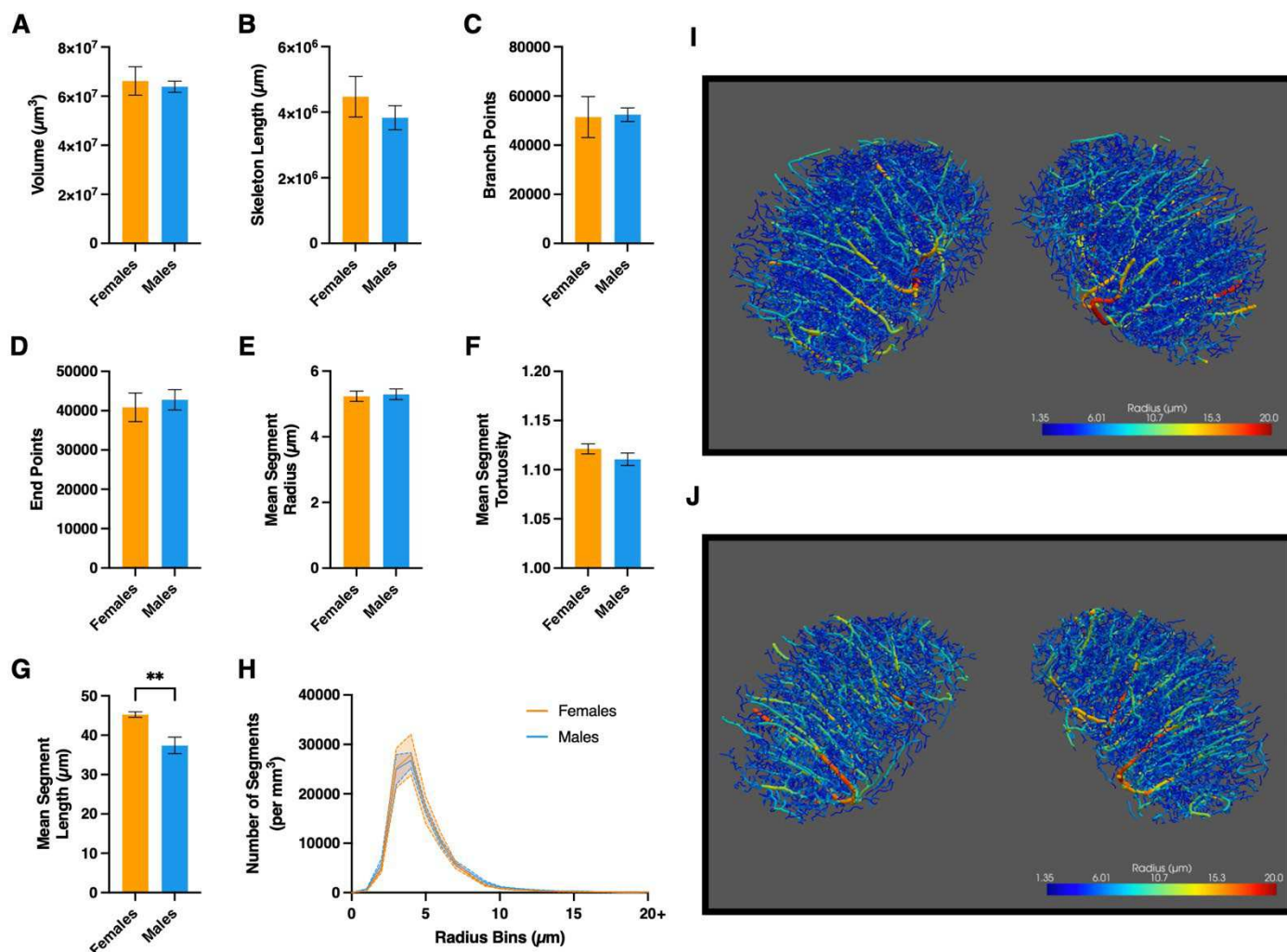


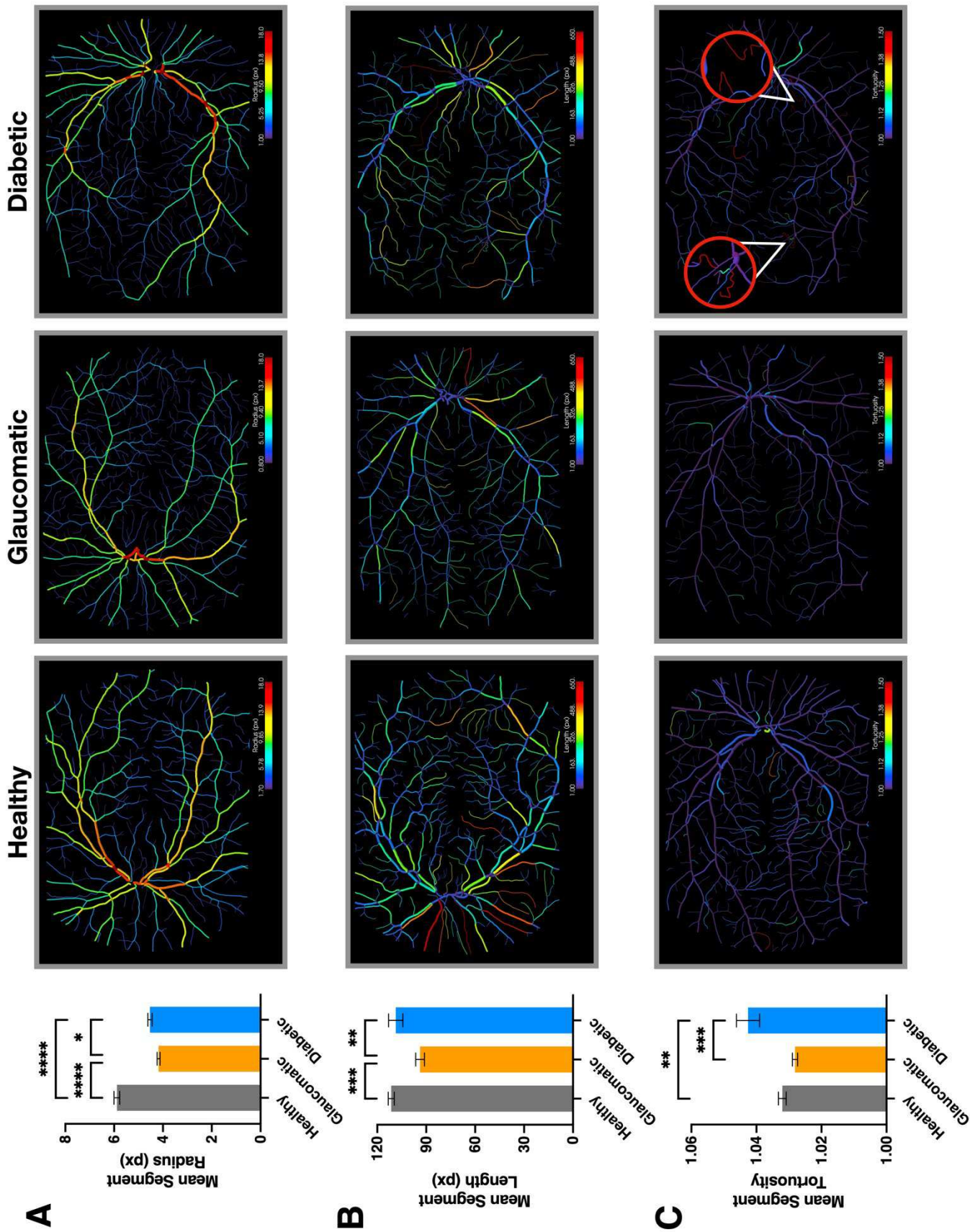
**Figure 3** – Results from the analysis of inferior colliculi segmentations from female and male CFW mice. **a-f**, Comparisons of network area (**a**), length (**b**), branch points (**c**), end points (**d**), mean segment length (**e**), mean segment tortuosity (**f**), and mean segment length (**g**). **h**, Distribution of the number of segments along 0-20+ radius bins. **i-j**, example images from female (**i**) and male (**j**) inferior colliculus reconstructions. Results for **a-d** and **h** were corrected by the region-of-interest volume for individual segmentations; these results are per  $\text{mm}^3$ . Data are represented as mean  $\pm$  SEM. **a-g**, Data analyzed using two-tailed student's t-test. **h**, Data analyzed using 2-way ANOVA;  $n = 5$ . \*\* -  $p < 0.01$ .

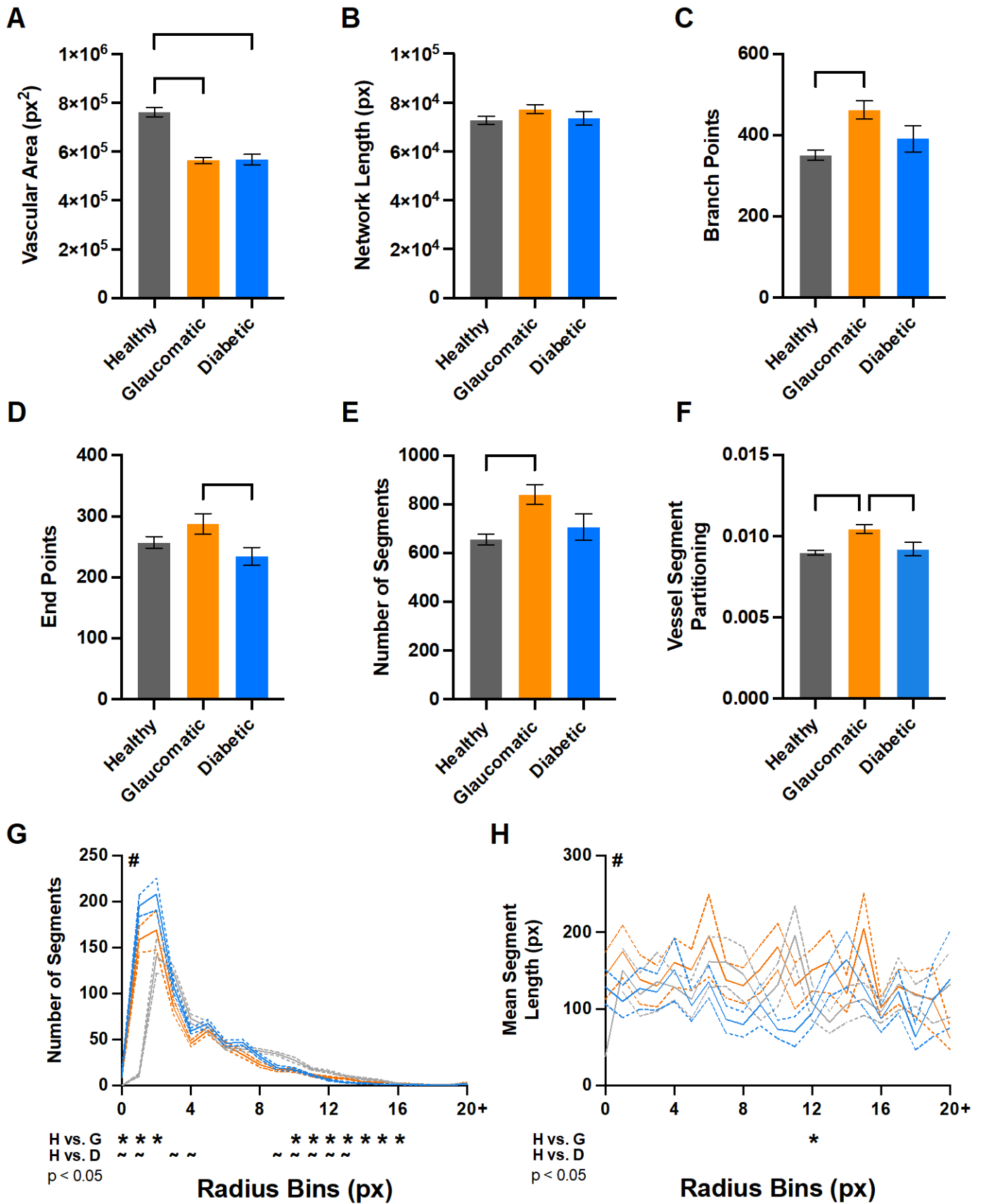
## 2D Retinography

215 To demonstrate the utility of VesselVio with 2D datasets, retinographs sourced from the HRF  
216 Image Database were analyzed and compared<sup>33</sup>. This database contains high-resolution images of  
217 healthy control patients, patients with diabetic retinopathy, and patients with glaucomatous eyes.  
218 VesselVio analysis revealed several differences among groups in the HRF database. Relative to  
219 healthy controls, diabetic patients present with reductions in vessel area (Figure 5A), reduced average  
220 segment radius (Figure 4A), and increased vessel tortuosity (Figure 4C). Further, relative to healthy  
221 controls, glaucomatous retinas had reduced vascular area (Figure 5A), increased branchpoints (Figure  
222 5C), more segments (Figure 5E), and reduced average segment length (Figure 4B). Differences in the  
223 distribution of vessel radii between healthy and glaucomatous/diabetic networks occurred both in small  
224 and medium diameter vessels (Figure 5G; Supplementary Data 4).

225 **Figure 4** – Segment characteristic comparisons among HRF groups. **a**, Alterations in the mean  
226 segment radius among groups. **b**, Differences in the mean segment length of vessels among groups.  
227 **c**, Alterations in the mean tortuosity of segments among the groups. Data are represented as mean  $\pm$   
228 SEM. Data were analyzed using a one-way ANOVA;  $n = 15$ . Upon main-effect observation, multiple  
229 comparisons were conducted using Tukey's test. \* -  $p < 0.05$ , \*\* -  $p < 0.01$ , \*\*\* -  $p < 0.001$ , \*\*\*\* -  $p <$   
230  $0.0001$ .  
231

232 **Figure 5** – Results from the analysis of images from the HRF database. **a-f**, Comparisons of network  
233 area (**a**), length (**b**), branch points (**c**), end points (**d**), segment counts (**e**), and segment partitioning (**f**).  
234 **e**, Distribution of segments across 0-20+ radius segment bins. **g**, Mean length of segments in each  
235 radius bin (length in px). Data are represented as mean  $\pm$  SEM. **a-f**, Data analyzed using a one-way  
236 ANOVA. **g-h**, Data analyzed using a two-way ANOVA;  $n = 15$ . Upon main-effect observation, multiple  
237 comparisons were conducted using Tukey's test. # - Main effect of health condition, \* -  $p < 0.05$ , \*\* -  $p$   
238  $< 0.01$ , \*\*\*\* -  $p < 0.0001$ .  
239





## 242 Discussion

243 Vascular networks can dictate and indicate states of health and disease<sup>34</sup>. Characterization of  
244 the structural and community properties of these networks can improve our understanding of disease  
245 phenotypes and may lead to improved disease identification techniques and treatments. We developed  
246 an open-source application, VesselVio, for the analysis and visualization of segmented 2D and 3D  
247 vasculature datasets. Focus was centered on constructing an analysis pipeline capable of producing  
248 quantitative characterizations of numerous whole-network and small-scale segment features. Ground-  
249 truth result comparisons and two primary analyses were conducted to demonstrate the accuracy and  
250 feasibility of VesselVio for vasculature analysis.

251 The first set of analyses examined sex-differences in the cerebrovasculature of female and male  
252 CFW mice. There are numerous known sex-differences in the cardiovascular system, including  
253 vascular tone<sup>35</sup>, microcirculation<sup>36</sup>, and blood-brain barrier function<sup>37,38</sup>. We sought to examine how the  
254 cerebrovascular network in a specific nucleus, the inferior colliculus (IC), may differ based on sex.  
255 Analysis revealed few overall differences in the vasculature of these nuclei, save for differences in  
256 average segment lengths. However, these results still serve to demonstrate 3D network analysis utility  
257 of VesselVio.

258 The second set of analyses examined retinal vascular networks of healthy controls, DR patients,  
259 and patients with glaucoma. Alterations in retinal microvascular networks are associated with vision  
260 loss<sup>34</sup>, and structural changes associated with excessive or reduced angiogenesis can also serve as  
261 indicators for underlying disease states<sup>39,40</sup>. Our analyses revealed numerous vascular differences  
262 among the groups, including alterations in branchpoint density, altered vascular area, and altered  
263 tortuosity in the two disease states. Our analyses recapitulated previously reported reduced vessel  
264 area and diameter in glaucomatous eyes<sup>41</sup>, as well as increased segment tortuosity of DR eyes<sup>42</sup>.

265 Contrasting results in DR eyes were noted compared to previous studies that reported increased vessel  
266 diameters<sup>43,44</sup>, whereas we and others observed decreased diameters<sup>45,46</sup>. However, these differences  
267 may be due to the vessel type (the HRF vessels are not separated by arterial/venous hierarchy) or  
268 vascular region analyzed. Although VesselVio is not intended to be used in any clinical diagnostic  
269 contexts, this analysis demonstrates the ability of this application to identify and characterize vascular  
270 network alterations in pathological conditions.

271 In common with most analytical program, the functionality of VesselVio is limited by the quality  
272 or resolution of the images that are loaded into the program. For example, if anisotropic datasets are  
273 loaded without pre-smoothing or blurring filters, then skeletonization of these datasets can produce  
274 erroneous segments. To adjust for these errors, the option to prune small, connected end-segments is  
275 included (Supplementary Video 5), but this pruning is unbiased and could hinder some types of  
276 analyses, such as angiogenesis measurements. Also, if holes or imaging artifacts are present in  
277 datasets, the skeletonization algorithm can produce unexpected results. Another limitation is that all  
278 VesselVio analyses are automated based on user-defined settings; this means the program cannot  
279 take user input for the creation of directed graphs and does not allow post-construction manual feature  
280 corrections. Although graph file export is provided, modifying the program for individual needs such as  
281 directed graph creation will require source code customization. However, open sourcing our code  
282 prioritizes transparency and customizability.

283 Future studies seeking to pinpoint detailed microvasculature alterations or broadly characterize  
284 regional vascular network features can employ the analytical and visualization components of  
285 VesselVio to obtain and enhance understanding of their results. In sum, VesselVio bridges the gap  
286 between modern vasculature imaging and dated analysis techniques by providing an optimized, open-  
287 source analysis pipeline and user-friendly application free for use.

288

289 **Methods**

290 **Animals**

291 All experiments were approved by the West Virginia University Institutional Animal Care and Use  
292 Committee, and animals were maintained in accordance with NIH Animal Welfare guidelines. Adult  
293 female and male CFW mice (7- to 8-weeks of age; strain #024; Charles River Laboratories, USA) were  
294 obtained and maintained under 14:10 light-dark cycles (lights on from 0500-1900 h). Following arrival,  
295 animals were given 1-week to acclimate to vivarium conditions before tissue collection. Food (2018  
296 Teklad; Envigo, USA) and reverse osmosis water were provided *ad libitum* throughout the entire  
297 duration of the housing.

298

299 **Vascular Corrosion Casting and  $\mu$ CT Imaging**

300 Vascular casts of mouse brains were created using resin corrosion casting method described  
301 previously<sup>8</sup>. Perfusions occurred in the light phase between 1200-1600 h. Prior to perfusion, mice were  
302 injected i.p. with 25 U of heparin (63739-931-28; McKesson Corporation, USA) in 250  $\mu$ L of saline and  
303 then deeply anesthetized with isoflurane (4% induction, 1.5% maintenance) and 0.4 L/min oxygen flow  
304 mixture. Following confirmation of complete anesthetization, mice were perfused intracardially at a flow  
305 rate of 4 mL/min first with 15 mL of 25 U/mL heparin in saline, followed by 15 mL of 4%  
306 paraformaldehyde (#416780030; Acros Organics, Belgium) in saline with a pH of 7.4, followed lastly  
307 with PU4ii resin (VasQTec, Switzerland) formulated exactly as directed by the manufacturer. Five days  
308 after perfusion, the craniums were decalcified with a 12-h wash of 5% formic acid (BDH4554; VWR  
309 International, USA), the brains were dissected, and remaining tissue was removed from the casts with  
310 two 12-h washes of 7.5% KOH (BDH7622; VWR International) at 35 °C. Casts were then rinsed with

311 three 1-hour Milli-Q water washes, and the cleaned casts were osmicated in a 1% solution of osmium  
312 tetroxide (#75632; Sigma Aldrich, USA) for 12-hours to allow for optimal x-ray diffraction during  $\mu$ CT  
313 scans. Casts were imaged on a SkyScan 1272 (Bruker, USA) at 50 kV/ 200  $\mu$ A with 360° rotations in  
314 step sizes of 0.17°, no filter, 900 ms frame exposures, and 4 frame averages/step to produce an  
315 isotropic voxel resolution of 2.7  $\mu\text{m}^3$ . Scan parameters were determined based on the manufacturers  
316 guidance to achieve optimal x-ray transmission through the sample. Scans were then reconstructed  
317 using NRecon (Bruker) with beam hardening corrections at 15%, ring artefacts reduction at 3,  
318 smoothing at 0, custom alignment compensations set for each sample, and 0.02-0.40 dynamic image  
319 ranges. Following reconstruction, the volumes were resliced coronally for inferior colliculi  
320 segmentations. Using interpolated polygonal tracing with CTAn (Bruker), inferior colliculi were manually  
321 segmented from bregma -4.9 to -5.4 using the lobule 2 of the cerebellar vermis as a landmark for  
322 bregma -4.9 (Supplementary Video 1)<sup>47</sup>. Scans, reconstructions, re-slicing, and inferior colliculi  
323 segmentations were all conducted using the Bruker SkyScan analysis software suite.

## 325 **Dataset Input and Processing Preparation**

326 Images are loaded into VesselVio using the Simple-ITK image reader to improve compatibility  
327 with various file formats<sup>48</sup>. It is important to note that VesselVio is only compatible with vascular datasets  
328 that have been pre-segmented and binarized. To ensure that datasets loaded into the program are  
329 prepared appropriately for subsequent analysis, we re-binarize all inputs with a threshold of 1 and  
330 convert the image stack or single image into a binarized contiguous array of 0-value background and  
331 1-value foreground elements. If images are not loaded in 8-bit grayscale, then this binarization to  
332 unsigned integers process can save memory during subsequent processing. All array processing in  
333 VesselVio is conducted with NumPy<sup>49</sup>.

334

## 335 **Volume Skeletonization and Centerline Extraction**

336 VesselVio employs the scikit-image<sup>50</sup> implementation of a widely used medial axis parallel  
337 thinning algorithm<sup>25</sup>. We selected this algorithm because it produces few erroneous branchpoint  
338 extensions, particularly when used with high-resolution datasets. This algorithm is also capable of  
339 thinning 2D and 3D datasets, making it optimal for analytical purposes. Following skeletonization, (n,  
340 3) or (n, 2) arrays are created containing Cartesian coordinate information of the location of all vessel  
341 centerlines.

342

## 343 **Radii Calculations**

344 Before the creation of the undirected graph, vessel centerline radii measurements are  
345 conducted. Previous publications focused on voxel/pixel vasculature analysis have utilized Euclidean  
346 distance transforms (EDT) on segmented vasculature images to find centerline radii<sup>7,51</sup>. These  
347 blanket-ed EDT methods find the Euclidean distance (ED) from the centerline point to the center of the  
348 nearest non-vessel neighbor point. However, an apparent unconsidered flaw in this traditional method  
349 is that finding the ED to the nearest non-vessel neighbor can overestimate the radius of the vessel if it  
350 is measured in single-dimension orientations from the centerline vessel. For example, given an isotropic  
351 voxel resolution of  $1 \mu\text{m}^3$ , a straight vessel that is 1 voxel thick should have a radius of  $0.5 \mu\text{m}$   
352 (Supplementary Figure 1). However, the traditional EDT method will record this vessel as having a  
353 radius of  $1 \mu\text{m}^3$ , doubling the apparent diameter. This is because ED measurements are calculated  
354 between the coordinates of the center of the centerline voxel and the *center* of its non-vessel neighbor.  
355 Radii inflations in traditional EDT measurements are less pronounced as vessels become larger, but  
356 small-diameter vessels can be binned incorrectly using this blanket-ed technique. Instead, the

357 calculation should be made to the *edge* of the nearest non-voxel neighbor if it is oriented single-  
358 dimensionally to the centerline point. Because of this, a modified EDT (mEDT) calculation was  
359 implemented that has 0.5-unit corrections for all neighbors oriented along single X, Y, or Z axis  
360 directions.

361 An argument could be made to calculate distance to the corner of the center pixel/voxel, but the  
362 edge was selected. Given the phenotypical tubular shape of vessels, EDT-based radii measurements  
363 are more appropriate for neighbors located along two- and three-dimensional orientations in 2D or 3D  
364 space. Thus, only radii measurements for nearest neighbors in 1D space are corrected (Supplementary  
365 Figure 1).

366 In previous publications, EDTs are applied to the entire image, and the centerline values are  
367 then extracted. However, this process is computationally expensive and leads to difficulty with making  
368 the intended 1D corrections. As such, the mEDT method only calculates the ED of centerline points to  
369 the nearest non-vessel neighbors, rather than transforming the entire image. Points in the previously  
370 constructed centerline coordinate arrays are used as seeds for the placement of expanding boxes that  
371 search centerline point neighborhoods for non-vessel neighbors. This box expands around a centerline  
372 point until at least four non-vessel neighbors are identified, rather than a single neighbor as with  
373 previous implementations. Then, rather than directly computing the ED (square root of sum of squared  
374 deltas) between the centerline point and neighbor (1), the user finds the absolute deltas of the centerline  
375 and neighbor coordinates and loads the deltas into an mEDT lookup table with precomputed and pre-  
376 corrected ED radius values (2). This lookup table is constructed to a user-specified maximum size and  
377 has half-pixel/-voxel unit corrections for all measurements along single X, Y, or Z axes (e.g., a delta  
378 array of [0,0,5] returns a 4.5 voxel distance).

$$d_{radius}(c, b) = \sqrt{\sum_{i=1}^n (c_i - b_i)^2} \quad (1) \quad d_{radius} = mEDT_{LUT}[|c_x - b_x|, |c_y - b_y|, |c_z - b_z|] \quad (2)$$

379

380

381

382

383

384

385

386

387

388

389

## Graph Construction

390

391

392

393

394

395

396

397

398

Following radii measurements, VesselVio constructs undirected graphs to represent the vasculature skeleton in an abstract space. To do this, the number of centerline points is identified, and an equal number of isolated vertices are added to the graph. Centerline points are assigned a vertex index based on their order of appearance in our point Cartesian coordinate array; these indices are then stored in a temporary lookup table used for edge creation in the graph. Further, each vertex is given a coordinate and radius attribute based on its corresponding point values. Next, the forward facing 13-connectivity neighborhood of all centerline points is scanned to identify immediate neighbors. Upon neighbor identification, an edge is created between the vertices. Unidirectional scanning in edge identification process prevents parallel edges from being created<sup>6</sup>.

399 Following graph creation,  $n \neq 2$  degree vertices are filtered from the graph. The remaining  
400 components are then scanned, and isolated segments and endpoint segments shorter than user-  
401 defined sizes are pruned (Supplementary Video 5). Following the removal of isolated segments from  
402 the graph, a custom flood-filling process is implemented to remove corresponding pixels/voxels from  
403 the original volume. Flood-filling of these isolated segments prevents inflation of the calculated  
404 area/volume. This technique is not implemented for endpoint segments, as endpoint segment pruning  
405 is used to remove erroneous centerlines created during skeletonization. From our tests, endpoint  
406 segments in need of pruning are often incorrectly skeletonized centerlines within large segments, so  
407 flood filling is not implemented for these segments.

408 Graphical representation of the vasculature construction also allows for improved identification  
409 of branchpoints. Branchpoints are often identified based on simple neighborhood connectivity; if a  
410 centerline point has more than two neighbors, it is defined as a branchpoint<sup>7,16</sup>. However, this method  
411 leads to an artificial inflation of identified branchpoints; this is because at branchpoint junctions, multiple  
412 vertices can have  $> 2$  neighbors – not just a single branchpoint. In graphical space, these falsely  
413 identified branchpoints form small loops, or cliques. To correct for this, we constructed a set of 12  
414 branchpoint filtering algorithms that remove  $>99\%$  of identified branchpoint cliques as determined by  
415 the datasets analyzed in this manuscript (Supplementary Data 1; Supplementary Video 6). Briefly,  
416 branchpoints are isolated from the main graph, and identified cliques are individually processed. A  
417 clique is classified based on its number of edges and branchpoints, and the appropriate filter is applied  
418 to identify the remaining branchpoint(s). Candidate branchpoints in the clique are positively weighted  
419 based on their radius, the radius of their neighbors, the degree of their connectivity. The highest  
420 weighted candidate(s) is/are then labelled as branchpoints, and the selected filter removes appropriate  
421 edges within the clique to eliminate branchpoint status of the lowest weighted candidate(s). The

pseudocode for these algorithms is in Supplementary text (Supplementary Notes), and all original code can be found at our GitHub page (<https://github.com/JacobBumgarner/VesselVio>).

Aside from area/volume measurements, all further individual segment characteristics and whole-network features are extracted from the constructed graph. Graph creation and processing in VesselVio uses the python igraph package<sup>53</sup>.

## Feature Extraction

Volume/area are measured by finding the number of voxels/pixels in the image after segment filtering. Branchpoint and endpoint counts are determined by the number of  $n > 3$  and  $n = 1$  degree vertices in the graph, respectively. Segments are identified in the graph by filtering  $n > 2$  degree vertices and then sorting through the remaining individual components. After each segment is identified, a mean segment radius is determined from the averaged vertices that construct the segment. Because calculating segment length based on vertex-vertex edges produces paths that are irregular to the vessel surface, a smoother path is constructed by creating a cubic B-spline from the coordinates of the original segment vertices using the geomdl package<sup>54</sup>. Quadratic B-splines are created for segments with 3 coordinate points. The length along the spline is then approximated using EDTs between a defined number of points along the spline identified using the *Cox-De Boor* algorithm<sup>54</sup>. Then, tortuosity measurements are created by finding the arc-cord ratio of the segment (segment length divided by the ED between the start and end points). Averages of segments are then created and automatically binned for ease of analysis. Segment partitioning is also calculated, which is the inverse of average segment length calculated by dividing the number of segments by the total network length<sup>55</sup>.

## Mesh Visualization and Application Interface

445 To construct meshes for visualization, we leverage the high-level python package PyVista<sup>56</sup> that  
446 wraps The Visualization Toolkit. We create individual poly-datasets from our segment splines, apply  
447 tube filters to create simple network and scaled network (based on average radius) meshes, and assign  
448 each tube a radius, length, and tortuosity scalar for visualization. All scalars and scaled segment sizes  
449 are based on the mean of segment features. These segments are combined into an undirected grid for  
450 surface extraction and subsequent rendering. Additional branchpoint and endpoint meshes are created.  
451 Then, original (voxel/pixel based) and smoothed surface meshes (marching cubes based-based) are  
452 created from the filtered input volume so researchers can visually validate the output features from the  
453 program by comparing simple/scaled networks to the original/smoothed meshes. Lastly, construction  
454 of the front-end application for VesselVio was accomplished with PyQt5 under GNU GPLv3 licensing  
455 (Supplementary Figure 2).

## 457 **Statistical Analysis**

458 All statistical analyses were conducted using Prism 9 (GraphPad; USA). Synthetic vasculature  
459 results were analyzed using one-way ANOVA tests and repeated-measures two-way ANOVA tests.  
460 HRF datasets were analyzed using one-way ANOVA tests. Mice IC data were analyzed using two-  
461 tailed student's t-tests. Distributions of segment counts per radii bin, average segment length per radii  
462 bin, and segment tortuosity per radii bin were all analyzed using two-way ANOVA tests. Following main  
463 effects observations in one- or two-way ANOVA tests, multiple comparisons were made using Tukey's  
464 test. An alpha of 0.05 was set for statistical significance.

## 466 **Data Availability**

467 The synthetic vasculature datasets and inferior colliculi segmentations analyzed in this article  
468 are available at the VesselVio Repository on the Harvard Dataverse website  
469 (<https://dataverse.harvard.edu/dataverse/VesselVio-Datasets>). All data generated in this manuscript  
470 are in the Supplementary files.

## 471

### 472 **Code Availability**

473 Original and updated source-code for VesselVio are available on GitHub  
474 (<https://github.com/JacobBumgarner/VesselVio>). Downloads for the MacOS and Windows standalone  
475 application can be found at the VesselVio homepage (<https://jacobbumgarner.github.io/VesselVio/>).  
476 Pseudocode for the branch point filtering algorithms is in the Supplementary Notes.

### 477

### 478 **Acknowledgements**

479 We acknowledge R.C. White for his assistance with corrosion cast generation and manuscript  
480 proofing. This project was supported by [National Institute of Health grant R01NS092388](#).  
481

### 482

### 483 **Author Contributions**

484 J.R.B. wrote the program source code, collected data, and analyzed data, J.R.B. and R.J.N. conceived  
485 the program, reviewed data analyses, and wrote and edited the manuscript.

### 486

### 487 **Competing Interests Statement**

488 The authors declare no competing interests.

## References

1. Teuwen L-A, Geldhof V, Pasut A, Carmeliet P. Covid-19: The vasculature unleashed. *Nat. Rev. Immunol.* **20**, 389-91 (2020).
2. Durham JT, Herman IM. Microvascular modifications in diabetic retinopathy. *Curr. Diabetes Rep.* **11**, 253-64 (2011).
3. Jiang X, Andjelkovic AV, Zhu L, Yang T, Bennett MVL, Chen J, Keep RF, Shi Y. Blood-brain barrier dysfunction and recovery after ischemic stroke. *Prog. Neurobiol.* **163**, 144-71 (2018).
4. Govindpani K, McNamara LG, Smith NR, Vinnakota C, Waldvogel HJ, Faull RLM, Kwakowsky A. Vascular dysfunction in alzheimer's disease: A prelude to the pathological process or a consequence of it. *J. Clin. Med.* **8**, 651 (2019).
5. Di Giovanna AP, Tibo A, Silvestri L, Müllenbroich MC, Costantini I, Mascaro ALA, Sacconi L, Frasconi P, Pavone FS. Whole-brain vasculature reconstruction at the single capillary level. *Sci. Rep.* **8**, 1-11 (2018).
6. Kirst C, Skriabine S, Vieites-Prado A, Topilko T, Bertin P, Gerschenfeld G, Verny F, Topilko P, Michalski N, Tessier-Lavigne M. Mapping the fine-scale organization and plasticity of the brain vasculature. *Cell.* **180**, 780-795. e25 (2020).
7. Todorov MI, Paetzold JC, Schoppe O, Tetteh G, Shit S, Efremov V, Todorov-Völggyi K, Düring M, Dichgans M, Piraud M. Machine learning analysis of whole mouse brain vasculature. *Nat. Methods.* **17**, 442-9 (2020).
8. Quintana DD, Lewis SE, Anantula Y, Garcia JA, Sarkar SN, Cavendish JZ, Brown CM, Simpkins JW. The cerebral angiome: High resolution microct imaging of the whole brain cerebrovasculature in female and male mice. *NeuroImage.* **202**, 116109 (2019).
9. Schaad L, Hlushchuk R, Barré S, Gianni-Barrera R, Haberthür D, Banfi A, Djonov V. Correlative imaging of the murine hind limb vasculature and muscle tissue by microct and light microscopy. *Sci. Rep.* **7**, 1-12 (2017).
10. Haft-Javaherian M, Fang L, Muse V, Schaffer CB, Nishimura N, Sabuncu MR. Deep convolutional neural networks for segmenting 3d in vivo multiphoton images of vasculature in alzheimer disease mouse models. *PLoS One.* **14**, e0213539 (2019).
11. Zudaire E, Gambardella L, Kurcz C, Vermeren S. A computational tool for quantitative analysis of vascular networks. *PLoS One.* **6**, e27385 (2011).
12. Niemisto A, Dunmire V, Yli-Harja O, Zhang W, Shmulevich I. Robust quantification of in vitro angiogenesis through image analysis. *IEEE Trans. Med. Imag.* **24**, 549-53 (2005).
13. Mazzaferri J, Larrivé B, Cakir B, Sapieha P, Costantino S. A machine learning approach for automated assessment of retinal vasculature in the oxygen induced retinopathy model. *Sci. Rep.* **8**, 1-11 (2018).
14. Montoya-Zegarra JA, Russo E, Runge P, Jadhav M, Willrodt A-H, Stoma S, Nørrelykke SF, Detmar M, Halin C. Autotube: A novel software for the automated morphometric analysis of vascular networks in tissues. *Angiogenesis.* **22**, 223-36 (2019).
15. Rust R, Kirabali T, Grönnert L, Dogancay B, Limasale YDP, Meinhardt A, Werner C, Laviña B, Kulic L, Nitsch RM. A practical guide to the automated analysis of vascular growth, maturation and injury in the brain. *Front. Neurosci.* **14**, 244 (2020).
16. Arganda-Carreras I, Fernández-González R, Muñoz-Barrutia A, Ortiz-De-Solorzano C. 3d reconstruction of histological sections: Application to mammary gland tissue. *Microsc. Res. Tech.* **73**, 1019-29 (2010).

- 536 17. Tetteh G, Efremov V, Forkert ND, Schneider M, Kirschke J, Weber B, Zimmer C, Piraud M,  
537 Menze BH. Deepvesselnet: Vessel segmentation, centerline prediction, and bifurcation detection  
538 in 3-d angiographic volumes. *Front. Neurosci.* **14**, (2020).
- 539 18. Hahn A, Bode J, Krüwel T, Solecki G, Heiland S, Bendszus M, Tews B, Winkler F, Breckwoldt  
540 MO, Kurz FT. Glioblastoma multiforme restructures the topological connectivity of  
541 cerebrovascular networks. *Sci. Rep.* **9**, 1-17 (2019).
- 542 19. Chapman BE, Berty HP, Schulthies SL. Automated generation of directed graphs from vascular  
543 segmentations. *J. Biomed. Inform.* **56**, 395-405 (2015).
- 544 20. Jafarnejad M, Ismail AZ, Duarte D, Vyas C, Ghahramani A, Zawieja DC, Celso CL,  
545 Poologasundarampillai G, Moore JE. Quantification of the whole lymph node vasculature based  
546 on tomography of the vessel corrosion casts. *Sci. Rep.* **9**, 1-11 (2019).
- 547 21. Epah J, Pálfi K, Dienst FL, Malacarne PF, Bremer R, Salamon M, Kumar S, Jo H, Schürmann C,  
548 Brandes RP. 3d imaging and quantitative analysis of vascular networks: A comparison of  
549 ultramicroscopy and micro-computed tomography. *Theranostics.* **8**, 2117 (2018).
- 550 22. Kelch ID, Bogle G, Sands GB, Phillips ARJ, LeGrice IJ, Dunbar PR. Organ-wide 3d-imaging and  
551 topological analysis of the continuous microvascular network in a murine lymph node. *Sci. Rep.*  
552 **5**, 1-19 (2015).
- 553 23. Selle D, Preim B, Schenk A, Peitgen H-O. Analysis of vasculature for liver surgical planning.  
554 *IEEE Trans. Med. Imag.* **21**, 1344-57 (2002).
- 555 24. Czech W, Dzwiniel W, Arodz T, Dudek AZ. Exploring complex networks with graph investigator  
556 research application. *Comput. Inform.* **30**, 381-410 (2011).
- 557 25. Lee T-C, Kashyap RL, Chu C-N. Building skeleton models via 3-d medial surface axis thinning  
558 algorithms. *CVGIP - Graph. Model. Im.* **56**, 462-78 (1994).
- 559 26. Palágyi K, Tschirren J, Hoffman EA, Sonka M. Quantitative analysis of pulmonary airway tree  
560 structures. *Comput. Biol. Med.* **36**, 974-96 (2006).
- 561 27. Chen Y, Laura CO, Drechsler K. Generation of a graph representation from three-dimensional  
562 skeletons of the liver vasculature. *2009 2nd International Conference on Biomedical Engineering  
563 and Informatics.* 1-5 (2009).
- 564 28. Tetteh G, Efremov V, Forkert ND, Schneider M, Kirschke J, Weber B, Zimmer C, Piraud M,  
565 Menze BH. Deepvesselnet: Vessel segmentation, centerline prediction, and bifurcation detection  
566 in 3-d angiographic volumes. *Front. Neurosci.* **14**, (2020).
- 567 29. Antiga L, Ene-Iordache B, Remuzzi A. Computational geometry for patient-specific  
568 reconstruction and meshing of blood vessels from mr and ct angiography. *IEEE Trans. Med.  
569 Imag.* **22**, 674-84 (2003).
- 570 30. Antiga L, Steinman DA. Robust and objective decomposition and mapping of bifurcating vessels.  
571 *IEEE Trans. Med. Imag.* **23**, 704-13 (2004).
- 572 31. Mouches P, Forkert ND. A statistical atlas of cerebral arteries generated using multi-center mra  
573 datasets from healthy subjects. *Sci. Data.* **6**, 1-8 (2019).
- 574 32. Bernier M, Cunnane SC, Whittingstall K. The morphology of the human cerebrovascular system.  
575 *Hum. Brain Mapp.* **39**, 4962-75 (2018).
- 576 33. Budai A, Bock R, Maier A, Hornegger J, Michelson G. Robust vessel segmentation in fundus  
577 images. *Int. J. Biomed. Imaging.* **2013**, (2013).
- 578 34. Carmeliet P. Angiogenesis in life, disease and medicine. *Nature.* **438**, 932-6 (2005).

- 579 35. Boese AC, Kim SC, Yin K-J, Lee J-P, Hamblin MH. Sex differences in vascular physiology and  
580 pathophysiology: Estrogen and androgen signaling in health and disease. *Am. J. Physiol. Heart*  
581 *Circ.* **313**, H524-45 (2017).
- 582 36. Huxley VH, Kemp SS in *Sex-Specific Analysis Of Cardiovascular Function* (eds Kerkhof PLM,  
583 Miller VM) 307-28 (Springer, New York City, 2018).
- 584 37. Robison LS, Gannon OJ, Salinero AE, Zuloaga KL. Contributions of sex to cerebrovascular  
585 function and pathology. *Brain Res.* **1710**, 43-60 (2019).
- 586 38. Humphries KH, Izadnegadar M, Sedlak T, Saw J, Johnston N, Schenck-Gustafsson K, Shah RU,  
587 Regitz-Zagrosek V, Grewal J, Vaccarino V. Sex differences in cardiovascular disease—impact on  
588 care and outcomes. *Front. Neuroendocrinol.* **46**, 46 (2017).
- 589 39. Lee R, Wong TY, Sabanayagam C. Epidemiology of diabetic retinopathy, diabetic macular  
590 edema and related vision loss. *Eye Vis.* **2**, 1-25 (2015).
- 591 40. Selvam S, Kumar T, Fruttiger M. Retinal vasculature development in health and disease. *Prog.*  
592 *Retin. Eye Res.* **63**, 1-19 (2018).
- 593 41. Chan KKW, Tang F, Tham CCY, Young AL, Cheung CY. Retinal vasculature in glaucoma: A  
594 review. *BMJ Open Ophthalmol.* **1**, e000032 (2017).
- 595 42. Sasongko MB, Wong TY, Nguyen TT, Cheung CY, Shaw JE, Wang JJ. Retinal vascular  
596 tortuosity in persons with diabetes and diabetic retinopathy. *Diabetologia.* **54**, 2409-16 (2011).
- 597 43. Bek T. Diameter changes of retinal vessels in diabetic retinopathy. *Curr. Diabetes Rep.* **17**, 1-7  
598 (2017).
- 599 44. Klein R, Myers CE, Lee KE, Gangnon R, Klein BEK. Changes in retinal vessel diameter and  
600 incidence and progression of diabetic retinopathy. *Arch. Ophthalmol.* **130**, 749-55 (2012).
- 601 45. Adhi M, Brewer E, Waheed NK, Duker JS. Analysis of morphological features and vascular  
602 layers of choroid in diabetic retinopathy using spectral-domain optical coherence tomography.  
603 *JAMA Ophthalmol.* **131**, 1267-74 (2013).
- 604 46. Fryczkowski AW, Sato SE, Hodes BL. Changes in the diabetic choroidal vasculature: Scanning  
605 electron microscopy findings. *Ann. Ophthalmol.* **20**, 299-305 (1988).
- 606 47. Paxinos G, Franklin KBJ. *Paxinos and Franklin's the mouse brain in stereotaxic coordinates*  
607 (Academic Press, Cambridge, 2019).
- 608 48. Lowekamp BC, Chen DT, Ibáñez L, Blezek D. The design of simpleitk. *Front. Neuroinform.* **7**, 45  
609 (2013).
- 610 49. Harris CR, Millman KJ, van der Walt SJ, Gommers R, Virtanen P, Cournapeau D, Wieser E,  
611 Taylor J, Berg S, Smith NJ. Array programming with numpy. *Nature.* **585**, 357-62 (2020).
- 612 50. Van der Walt S, Schönberger JL, Nunez-Iglesias J, Boulogne F, Warner JD, Yager N, Gouillart  
613 E, Yu T. Scikit-image: Image processing in python. *PeerJ.* **2**, e453 (2014).
- 614 51. Tsai PS, Kaufhold JP, Blinder P, Friedman B, Drew PJ, Karten HJ, Lyden PD, Kleinfeld D.  
615 Correlations of neuronal and microvascular densities in murine cortex revealed by direct  
616 counting and colocalization of nuclei and vessels. *J. Neurosci.* **29**, 14553-70 (2009).
- 617 52. Lam SK, Pitrou A, Seibert S. Numba: A llvm-based python jit compiler. *Proceedings of the*  
618 *Second Workshop on the LLVM Compiler Infrastructure in HPC.* **7**, 1-6 (2015).
- 619 53. Csardi G, Nepusz T. The igraph software package for complex network research. *Int. J.*  
620 *Complex Syst.* **1695**, 1-9 (2006).
- 621 54. Bingol OR, Krishnamurthy A. Nurbs-python: An open-source object-oriented nurbs modeling  
622 framework in python. *SoftwareX.* **9**, 85-94 (2019).

623  
624  
625  
626  
627

55. Corliss BA, Mathews C, Doty R, Rohde G, Peirce SM. Methods to label, image, and analyze the complex structural architectures of microvascular networks. *Microcirculation*. **26**, e12520 (2019).
56. Sullivan CB, Kaszynski AA. Pyvista: 3d plotting and mesh analysis through a streamlined interface for the visualization toolkit (vtk). *J. Open Source Softw.* **4**, 1450 (2019).

# Supplementary Files

This is a list of supplementary files associated with this preprint. Click to download.

- [SupplementaryNotes.docx](#)
- [SupplementaryData1CliqueFilteringResults.xlsx](#)
- [SupplementaryData2mEDTvsEDTDistributionResults.xlsx](#)
- [SupplementaryData3ICResults.xlsx](#)
- [SupplementaryData4HRFResults.xlsx](#)
- [SupplementaryFigure1EDTvsEDT.docx](#)
- [SupplementaryFigure2ApplicationImages.docx](#)
- [SupplementaryVideo1ICSegmentation.mov](#)
- [SupplementaryVideo2InferiorColliculusOrbits.mov](#)
- [SupplementaryVideo3LSMDatasets.mov](#)
- [SupplementaryVideo4LeftHemisphereofToFSWIComposite.mov](#)
- [SupplementaryVideo5BranchPruning.mov](#)
- [SupplementaryVideo6BranchPointFiltering.mov](#)